



## Custom plating of nanoscale semiconductor/catalyst junctions for photoelectrochemical water splitting

Kiseok Oh, Olivier de Sagazan, Cyril Léon, Sylvain Le Gall, Gabriel Loget

### ► To cite this version:

Kiseok Oh, Olivier de Sagazan, Cyril Léon, Sylvain Le Gall, Gabriel Loget. Custom plating of nanoscale semiconductor/catalyst junctions for photoelectrochemical water splitting. *Nanoscale*, 2021, 13 (3), pp.1997-2004. 10.1039/D0NR08414J . hal-03100848

**HAL Id: hal-03100848**

**<https://hal.science/hal-03100848>**

Submitted on 11 Jan 2021

**HAL** is a multi-disciplinary open access archive for the deposit and dissemination of scientific research documents, whether they are published or not. The documents may come from teaching and research institutions in France or abroad, or from public or private research centers.

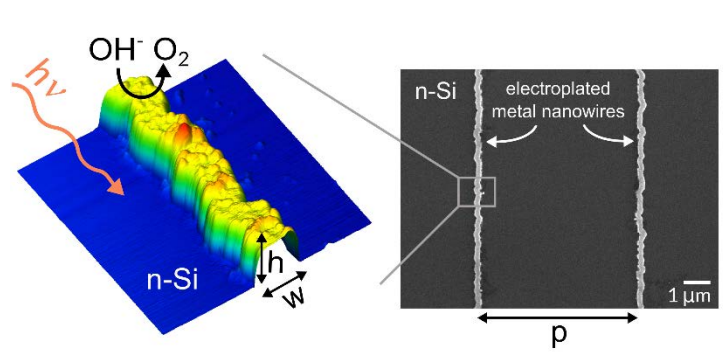
L'archive ouverte pluridisciplinaire **HAL**, est destinée au dépôt et à la diffusion de documents scientifiques de niveau recherche, publiés ou non, émanant des établissements d'enseignement et de recherche français ou étrangers, des laboratoires publics ou privés.

# Custom plating of nanoscale semiconductor/catalyst junctions for photoelectrochemical water splitting

Kiseok Oh,<sup>a</sup> Olivier de Sagazan,<sup>b</sup> Cyril Léon,<sup>c</sup> Sylvain Le Gall,<sup>c\*</sup> Gabriel Loget<sup>a\*</sup>

- a. Univ Rennes, CNRS, ISCR (Institut des Sciences Chimiques de Rennes)-UMR6226, F-35000 Rennes, France. [gabriel.loget@univ-rennes1.fr](mailto:gabriel.loget@univ-rennes1.fr)
- b. Univ Rennes, CNRS, IETR (Institut d'Électronique et des Télécommunications de Rennes)-UMR6164, F-35000 Rennes, France.
- c. Group of Electrical Engineering-Paris (GeePs) CNRS, CentraleSupélec, Univ. Paris-Saclay, Sorbonne Univ., 11 rue Joliot-Curie, 91192, Gif-sur-Yvette France. [sylvain.le-gall@u-psud.fr](mailto:sylvain.le-gall@u-psud.fr)

Photoelectrochemical water splitting under harsh chemical conditions can be promoted by dispersed transition metal nanoparticles electrodeposited on n-Si surfaces, without the need for classical protection layers. Although this method is simple, it only allows for poor control of metal morphology and geometry on the photoanode surface. Herein, we introduce templated nanoscale electrodeposition on photoactive n-Si for the customization of nanoscale inhomogeneous Schottky junctions and demonstrate their use as stable photoanodes. The photoelectrochemical properties of the so-manufactured photoanodes exhibit a strong dependence on the photoanodes' geometrical features, and the obtained experimental trends are rationalized using simulation.



## INTRODUCTION

The sun is an infinite source of natural energy, inexhaustible for more than 4 billion years. However, efficient harvesting of solar energy with a minimal footprint is still a significant challenge that is driving intense scientific research, especially in the context of climate change.<sup>1,2</sup> Several technologies have been developed for capturing and storing sunlight energy. Among these technologies, photoelectrochemical cells (PECs) are inspired by photosynthesis and convert sunlight into energy-rich  $H_2$  by dissociating water.<sup>3-5</sup> In this technology, semiconductor (SC) surfaces (i.e., photoelectrodes) are immersed in water to promote hydrogen evolution reaction (HER) and oxygen evolution reaction (OER) through the transfer of photogenerated charges at the solid/liquid interface.<sup>6,7</sup> PEC systems require an efficient utilization of sunlight, which can be ideally achieved by employing a small bandgap SC or tandem heterojunctions.<sup>8,9</sup> Si is Earth-abundant, has a low bandgap ( $E_g = 1.1$  eV), has high charge carrier mobilities, has low recombination rates, and is commonly processed at the industrial level, which makes it a perfect candidate for manufacturing PECs.<sup>10,11</sup> The photoanode is a clearly identified bottleneck of Si-based PECs, as Si strongly suffers from photocorrosion<sup>12</sup> and chemical etching<sup>13</sup> in high-pH electrolytes.<sup>14</sup> Moreover, the immobilization of a catalytic coating at the outermost surface of the photoanode is always required to improve the otherwise slow OER kinetics.<sup>15</sup> These constraints can be solved by introducing protecting and catalytic layers, which typically consist of thin films deposited on Si by physical vapor deposition (PVD) methods, such as sputtering or atomic layer deposition (ALD).<sup>16-23</sup>

An alternative low-cost strategy<sup>24</sup> bases on inhomogeneous  $n$ -Si/M NPs Schottky junctions (where M = Ni,<sup>25-28</sup> Co,<sup>29,30</sup> and Fe<sup>31</sup>), which are prepared by the simple electrodeposition of transition metal nanoparticles (M NPs) from an aqueous solution onto  $n$ -Si and can be directly employed as stable Si-based photoanodes (typical stabilities:  $>10$  h<sup>32</sup> and  $>300$  h<sup>33</sup> at pH  $\sim 14$  and  $\sim 9$ , respectively) without the need for the deposition of a conformal layer. A typical  $n$ -Si/Ni NP photoanode produced by this method is shown in **Figure 1a**. During operation of such systems, a protective  $SiO_x$  layer at the Si surface and a hydroxide-oxyhydroxide ( $M(OH)_2$ -MOOH) shell on the metal NPs grant stability and promote high OER activity, respectively.<sup>32</sup> These photoanodes are described as inhomogeneous junctions operating in the “pinch-off” regime, as illustrated in Figure 1b.<sup>24,35</sup> Herein, a mixed contact is established between  $n$ -Si and *i*) a low barrier height ( $q\phi_m$ ) region and *ii*) a high barrier height ( $q\phi_h$ ) region. Although it has been demonstrated that the low barrier height region results from the metal contact  $n$ -Si/M due to Fermi level pinning,<sup>29,36,37</sup> the nature of the high barrier height region ( $n$ -Si/ $SiO_x$ ,<sup>36</sup>  $n$ -Si/ $M(OH)_2$ ,<sup>33</sup>  $n$ -Si/MOOH<sup>37</sup>, or  $n$ -Si/ $MO_x$ <sup>26</sup>) is still discussed in the literature.<sup>24,29</sup> It has been shown that when the characteristic size of the M NP is comparable or smaller than the depletion width ( $W \sim 10$ – $1000$  nm), the distinct regions act no longer as parallel contacts and the minority carriers experience a higher effective barrier height ( $q\phi_{eff}$ ; Figure 1b).<sup>34,35</sup> The pinch-off effect is extremely beneficial because it takes advantage of the  $q\phi_h$  region to generate a high photovoltage and the  $n$ -Si/M region to create a low resistance pathway for photogenerated minority carriers, which are readily injected at the catalytic surface for OER (Figure 1a). To date,  $n$ -Si/M NPs photoanodes, such as  $n$ -Si/Ni NPs, are only produced by conventional metal electrodeposition.<sup>25-31</sup> While this approach is very attractive due to its simplicity and cost, it is based on a process that involves randomly-dispersed nucleation, which does not allow fine control over the geometrical parameters of the nanoscale  $n$ -Si/M junction and produces M NPs with a broad dispersion in diameter<sup>25</sup> and shape.<sup>29,31</sup> By this method, the dimensions of the metal contacts can be hardly controlled, which is critical for promoting pinch-off and reaching high photoelectrochemical performance. Furthermore, control of the respective spacing between the metallic NPs is difficult.

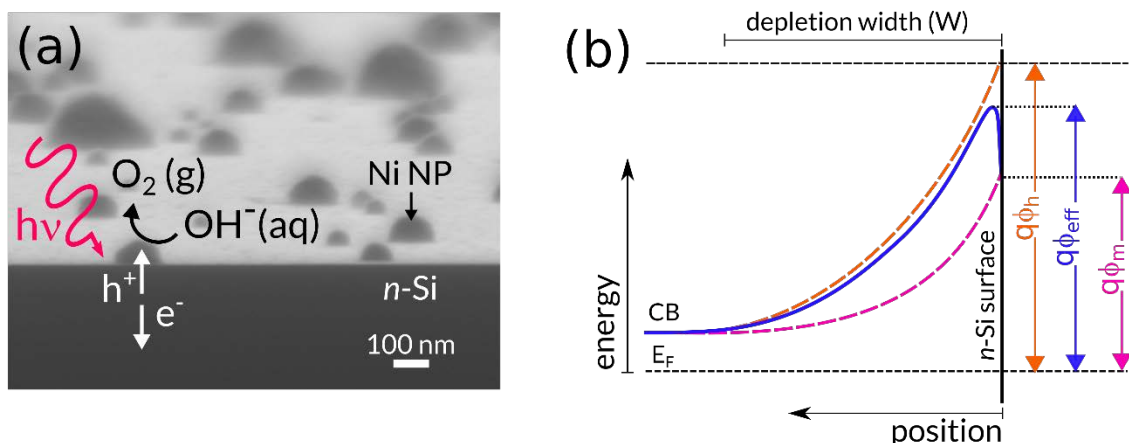


**Figure 1.** (a) Tilted SEM view of an  $n$ -Si/Ni NP photoanode prepared by conventional electrodeposition of Ni on  $n$ -Si. The left part of the panel illustrates the photoanode operation in alkaline pH. Under illumination, holes are directed to the Ni NPs where they participate in the OER reaction. (b) Scheme of the conduction band energy as a function of the position in  $n$ -Si in the pinch-off regime (adapted from ref. 34), where  $q\phi_m$  is the low barrier height at the metal contact,  $q\phi_h$  is the high barrier height, and  $q\phi_{eff}$  is the effective barrier height.

Lithographically patterned nanowire electrodeposition (LPNE) is a convenient manufacturing process developed by Penner *et al.*<sup>38,39</sup> that has been employed to the electrodeposition of metal nanowires (M NWs) on dielectrics, such as glass slides<sup>40</sup> or polymer films<sup>41</sup>, to create nanostructured surfaces, which have been applied in gas sensing<sup>42</sup> and capacitors.<sup>43</sup> The linear NW geometry is particularly interesting for photoelectrochemistry applications, because it is expected to promote pinch-off as observed for hemispherical NPs (exemplarily shown in Figure 1a) according to predictions by Tung *et al.*<sup>44,45</sup>

In this article, we used LPNE for the electrodeposition of catalytic transition metal nanowires (M NWs) with high aspect ratio onto photoactive  $n$ -Si. We show that this new approach allows a high degree of control over the geometrical features and the spacing of the nanoscale junctions. Moreover, we demonstrate that this original method can be employed for the design of OER-active and stable photoanodes with high spatial control, and we study the influence of the geometrical parameters on photoelectrochemical OER at  $n$ -Si/Ni NWs. We finally employed an electrical modeling approach to qualitatively understand our results. The degree of control provided by this approach has the potential to open up new perspectives for photoelectrodes based on nanoscale  $n$ -Si/M junctions.

## Results and Discussion

### Composition and morphology control of $n$ -Si/M NW surfaces

**Figure 2a** shows the different fabrication steps of lithographically patterned nanowire electrodeposition (LPNE), which combines the advantages of photolithography, providing control over the structuration of the array at the micrometer scale, with those of electrochemistry, providing the fine-tuning of the dimension of each nanostructure at the nanoscale in a parallel manner.<sup>38-40</sup>

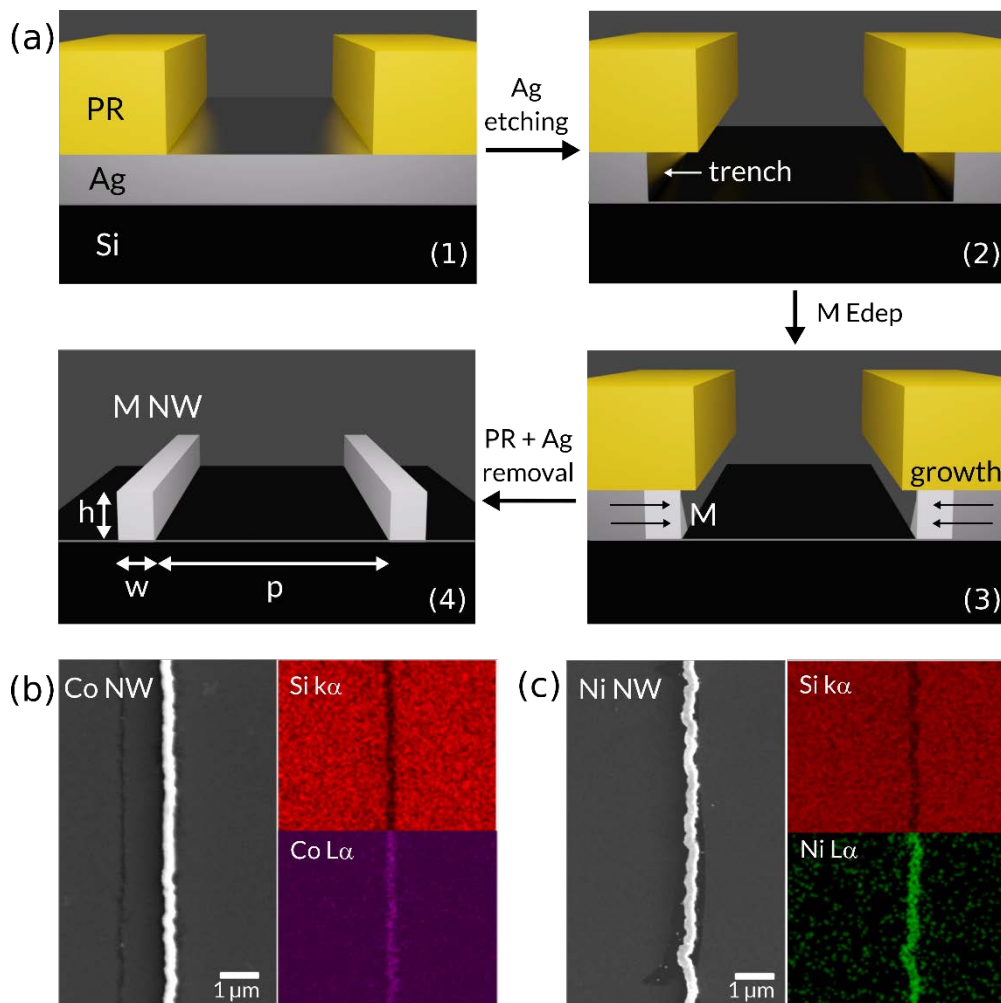


**Figure 2.** (a) Scheme of the sequential steps of templated electrodeposition for the preparation of catalytic metal NWs with a high degree of control. The metal growth direction is indicated by black arrows in panel 3, and the geometrical parameters  $h$ ,  $w$ , and  $p$  are shown in panel 4. (b,c) SEM top views (left panels) and corresponding Si  $K\alpha$  (red), Co  $L\alpha$  (pink), and Ni  $L\alpha$  (green) EDS mapping (right panels) of electrodeposited (b) Co NWs and (c) Co NWs on  $n$ -Si.

First, lightly doped  $n$ -Si(100) surfaces (resistivity = 1–10  $\Omega$  cm) were covered by a ~80-nm-thick sacrificial Ag thin film and coated by a photoresist (PR) layer that was patterned with stripes over 0.5 x 0.5 cm<sup>2</sup> by photolithography (Figure 2a, panel (1)). In the following, this surface will be referred to as “template”. Then, the unprotected Ag layer was chemically etched by an NH<sub>4</sub>OH/H<sub>2</sub>O<sub>2</sub> mixture to create trenches between the Si substrate and the PR (Figure 2a, panel 2). After that, an electrical contact was established on the Ag layer (note that all Ag stripes were electrically connected according to Figure S1) for the aqueous electrodeposition of a transition metal M (Figure 2a, panel 3). In this step, electrodeposition is expected to only occur at the surface of the metal layer that is in contact with the electrodeposition bath due to the electrical resistance of the Si wafer and the rectifying nature of the  $n$ -Si/Ag junction<sup>46</sup> (as a first approximation), i.e., the Ag surface recessed within the nanoscale trench. This leads to the lateral growth of the metal deposit onto the edges of the silver stripes (black arrows in Figure 2a, panel 3). Finally, the PR is dissolved by acetone, and Ag is selectively etched away, exposing the aligned M NWs on the Si surface (Figure 2a, panel 4). This technique allows the tailored patterning of  $n$ -Si with electrodeposited catalytic M NW arrays over a large surface (0.5 x 0.5 cm<sup>2</sup>). The shape, number, and corresponding pitch ( $p$ ) of the NWs were

controlled by the photomask used to create the template (Figure 2a, panel 1), while the height ( $h$ ) and width ( $w$ ) of individual NWs were controlled by the thickness of the sacrificial layer and the electrodeposition parameters (Figure 2a, panel 3). To the best of our knowledge, LPNE has not been previously used on photoactive Si. Furthermore, such a geometry has never been employed for water splitting, even if it has been predicted as promising.<sup>44,45</sup>

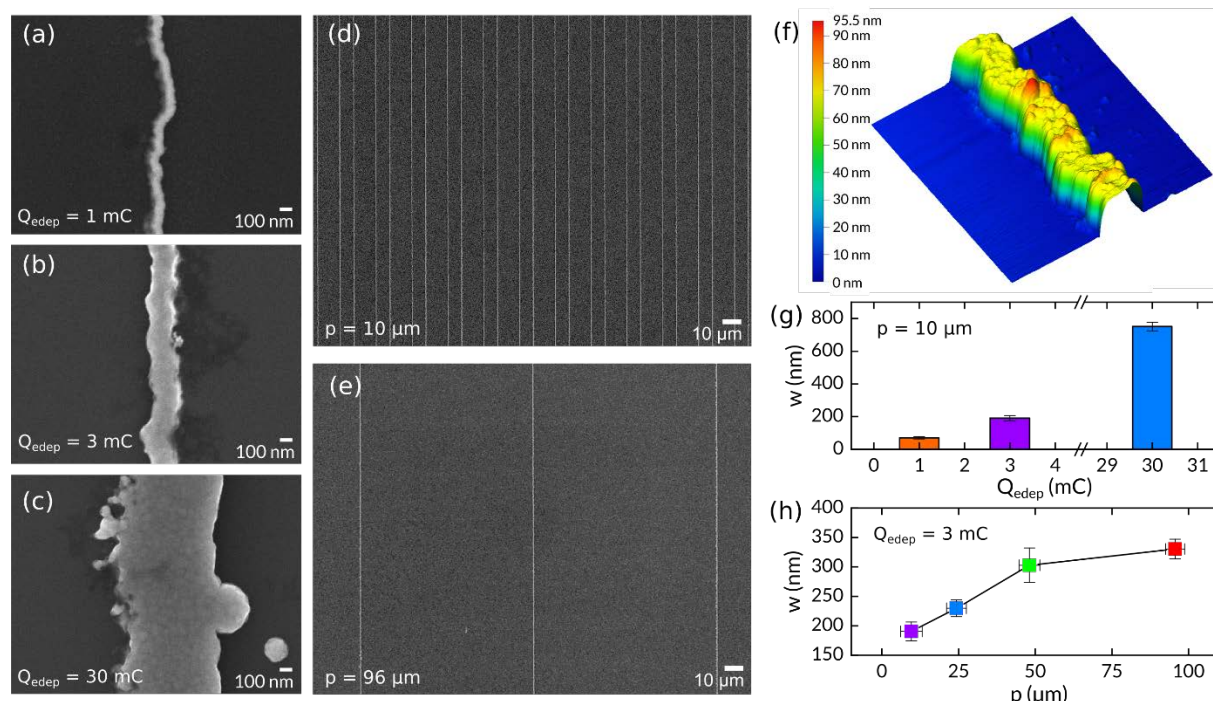


**Figure 3.** (a–c) High-magnification SEM top view images of Ni NWs electrodeposited on  $n$ -Si with  $p = 10 \mu\text{m}$  for (a)  $Q_{\text{edep}} = 1 \text{ mC}$ , (b)  $3 \text{ mC}$ , and (c)  $30 \text{ mC}$ . (d,e) Low-magnification SEM top view images of Ni NWs electrodeposited on  $n$ -Si with  $Q_{\text{edep}} = 3 \text{ mC}$  for (d)  $p = 10$  and (e)  $96 \mu\text{m}$ . (f) AFM picture ( $2 \times 2 \mu\text{m}^2$ ) of a single Ni NWs electrodeposited on  $n$ -Si. (g) Graph of  $w$  as a function of  $Q_{\text{edep}}$  for  $n$ -Si/Ni NWs prepared with  $p = 10 \mu\text{m}$ . (h) Plot of  $w$  as a function of  $p$  for  $n$ -Si/Ni NWs prepared with  $Q_{\text{edep}} = 3 \text{ mC}$ .

To assess the versatility of LPNE, we first tested it for the electrodeposition of the three transition metals (Fe, Co, and Ni). These materials were chosen as they are currently attracting considerable scientific attention as promising inexpensive and efficient catalysts for OER in alkaline medium<sup>14</sup> and also because they are known to yield efficient catalytic inhomogeneous  $n$ -Si/M NPs Schottky junctions<sup>25,29,30</sup> when electrodeposited as randomly-dispersed NPs on  $n$ -Si. The composition of the electrodeposition baths and the description of the electroplating methods are reported in the Supporting Information. Using LPNE, arrays of aligned Fe, Co, and Ni NWs were successfully obtained on  $n$ -Si by applying an electrodeposition charge ( $Q_{\text{edep}}$ ) of  $3 \text{ mC}$ . Scanning electron microscopy (SEM; Figure S2) revealed that the NWs had a width in the range of  $100 \text{ nm}$ , were continuous over long distances, and presented a good adhesion on the substrate. However, the Fe NWs (Figure S2) had an irregular border at one edge (i.e., the NW edge that faced the electrolyte side during electrodeposition (Figure 2a panel 3)), which was not the case for the better defined Co and Ni NWs, as revealed by SEM (Figure 2b,c). Energy-dispersive X-ray spectroscopy (EDS) was also performed, and the intensity mappings of Si  $\text{K}\alpha$  and  $\text{L}\alpha$  of the deposited transition metals confirmed the chemical nature of the M NWs (top and bottom rows of Figures 2b,c and S2c, respectively). Based on these tests and due to the higher expected stability of  $n$ -Si/Ni<sup>32</sup> compared to  $n$ -Si/Co<sup>29</sup> and  $n$ -Si/Fe<sup>31</sup> OER photoanodes in highly alkaline solution, we focused on the  $n$ -Si/Ni NW system in the following.

To evaluate the potential of nanoscale control of LPNE, we fixed the template, which was manufactured using a photomask with PR stripes of equal width and pitch (PR width  $p = 10 \mu\text{m}$ ), and



changed  $Q_{\text{edep}}$  by controlling the electrodeposition time to vary the Ni NW width. As shown in **Figure 3a–c** (additional SEM images are shown in Figures S3 and S4a), thin and continuous Ni NWs with a  $w$  value as low as  $71 \pm 7$  nm were obtained by decreasing  $Q_{\text{edep}}$  to 1 mC (Figure 3g, orange bar). In contrast, increasing  $Q_{\text{edep}}$  to 30 mC produced Ni NWs that were more than 10 times wider ( $w = 751 \pm 26$  nm; Figure 3g, blue bar). However, to our surprise, applying such a high charge during electrodeposition also induced the growth of randomly dispersed hemispherical Ni NPs (Figure S3a), which were similar to those obtained for  $n$ -Si/Ni NP photoanodes prepared by conventional electrodeposition (Figure 1a). The origin of the charge-specific nucleation of these NPs is still unclear and is currently under investigation in our laboratory.

In the next experiments, Ni NWs were prepared by applying a constant electrodeposition charge ( $Q_{\text{edep}} = 3$  mC) to four different templates, each manufactured using a photomask with PR stripes of equal pitch and width but with four different values (PR width = PR pitch = 10, 25, 50, or 100  $\mu\text{m}$ ). The resulting  $n$ -Si/Ni NW surfaces were characterized by SEM (Figure S4). Figure 3d,e shows the results obtained for PR width and pitch of 10 and 100  $\mu\text{m}$ , respectively, revealing that the Ni NWs were properly deposited and continuous over a length of  $>100$   $\mu\text{m}$ . Atomic force microscopy (AFM; Figures 3f and S5) revealed an  $h$  value of  $80 \pm 8$  nm. The  $p$  and  $w$  values of Ni NWs were measured from low and high-magnification SEM images, respectively. Although the width and the spacing of the PR stripes patterned for manufacturing the template were equal, the etching step of the preparation method (Figure 2a, panel 2) inherently induced a break in the  $p$  value between sequential Ni NWs. For the four  $n$ -Si/Ni NW surfaces, we experimentally determined  $p$  values of  $9.6 \pm 3.5$ ,  $24.3 \pm 3.2$ ,  $48.1 \pm 3.4$ , and  $95.6 \pm 3.1$   $\mu\text{m}$ , which are referred to by their rounded values (10, 24, 48, and 96  $\mu\text{m}$ , respectively) for simplicity in the following. As  $h$  remains constant, and  $p$  controls the number of recessed Ag nanobands on the surface, applying a constant  $Q_{\text{edep}}$  should ideally control the quantity of electrodeposited Ni atoms and, thus, affect  $w$  when using templates with distinct  $p$  values. This relation is depicted in Figure 3h, which shows that  $w$  increases from 190 to 330 nm for  $p$  varying from 10 to 96  $\mu\text{m}$ . Several sets of these surfaces were manufactured, prepared as electrodes, and studied for photoelectrochemical OER.

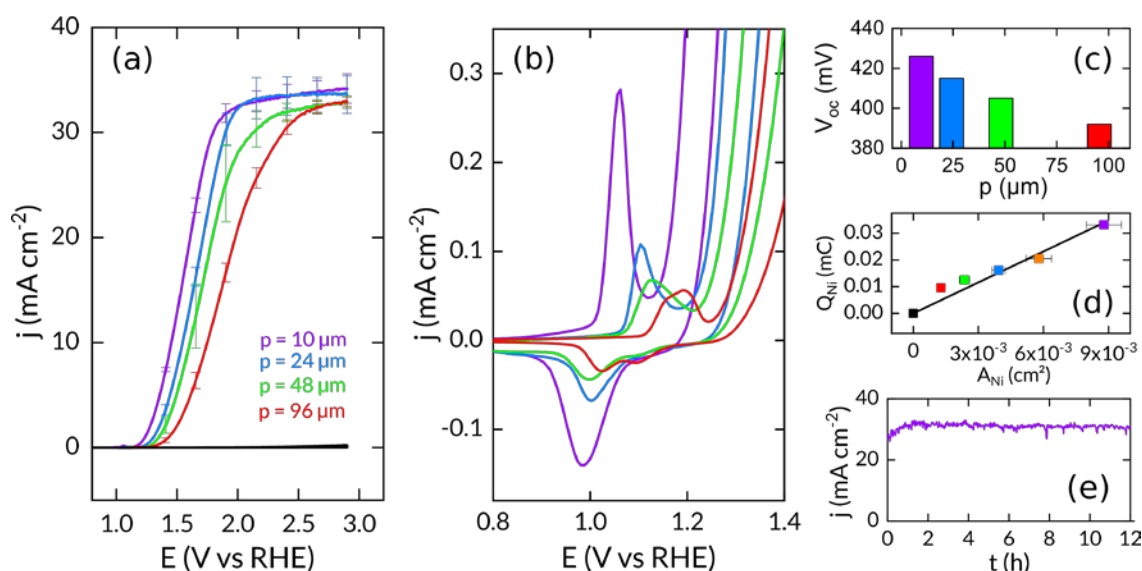


**Figure 4.** (a) LSVs (scan rate: 100  $\text{mV s}^{-1}$ ) of  $n$ -Si/Ni NWs in 1 M NaOH with different  $p$  values, constant electrodeposition charge ( $Q_{\text{edep}} = 3$  mC), in the dark (black curves), and under illumination (colored curves, average of  $>3$  independently prepared samples). (b) CVs of  $\text{Ni}^{\text{III}}/\text{Ni}^{\text{II}}$  (scan rate: 100  $\text{mV s}^{-1}$ ) on  $n$ -Si/Ni NWs in 1 M NaOH under illumination. (c)  $V_{\text{OC}}$  values obtained by OCP measurements in a  $\text{Fe}^{\text{III}}(\text{CN})_6^{3-}/\text{Fe}^{\text{II}}(\text{CN})_6^{4-}$  solution. (d) Plot of  $Q_{\text{Ni}}$  as a function of  $A_{\text{Ni}}$ ; squares are experimental data points and the black curve is a linear fit. (e) CA of an  $n$ -Si/Ni NW at 2.3 V vs RHE ( $Q_{\text{edep}} = 3$  mC,  $p = 10$   $\mu\text{m}$ ) in K-borate/Li-borate buffer under illumination. In all panels, the color of the curves and the data points correspond to  $p = 10$  (purple), 24 (blue), 48 (green), and 96  $\mu\text{m}$  (red).

## Solar-assisted OER on *n*-Si/Ni NW photoanodes

As LPNE involves several preparation steps and the use of a sacrificial metal layer, we first had to ensure that any photoelectrochemical activity is only induced by M NWs. To this goal, a control sample was subjected to the same preparation process (Figure 2a) except the Ni electrodeposition step and tested photoelectrochemically, and showed a negligible photoresponse (Figure S10). In contrast, all *n*-Si/M NW photoelectrodes comprising Fe, Co, and Ni NWs exhibited a clear OER photoelectrochemical activity (Figure S11). These experiments demonstrated the absolute necessity of the presence of the deposited metal on the surface and that the measured activity did not originate from deleterious surface modification or impurities linked to the preparation process. As proof-of-principle comparative experiments, the electrochemical activity of *n*-Si/Ni NW surfaces prepared with  $Q_{\text{edep}} = 3 \text{ mC}$  and  $p = 10, 24, 48, \text{ and } 96 \mu\text{m}$  was studied by voltammetry in 1 M NaOH, as shown in **Figure 4a,b**. In the dark, the anodic activity was negligible (black curves). However, the four surfaces exhibited intense anodic photocurrents when illuminated from the frontside (through the electrolyte) with simulated sunlight (AM 1.5 G,  $100 \text{ mW cm}^{-2}$ ). The photoelectrochemical features of the *n*-Si/Ni NW photoanodes are in good agreement with those described for conventional inhomogeneous *n*-Si/Ni photoanodes.<sup>32,36</sup>

In particular, the performance of the *n*-Si/Ni NWs gradually improved during sequential voltammetry cycles (Figure S6) due to the oxidation of the Ni surface to  $\text{Ni}(\text{OH})_2\text{-NiOOH}$  and the doping of this outermost part by catalytically active adventitious Fe atoms.<sup>47,48</sup> This phenomenon, which has been previously reported and studied in detail,<sup>32,36</sup> is referred to as “activation”. Unless otherwise specified, all voltammetry curves reported in this article correspond to the 30<sup>th</sup> cyclic voltammetry (CV) cycle. For comparison, the OER activity of the four surfaces is shown in Figure 4a, revealing that their geometrical parameters do not significantly influence the light-limited photocurrent density ( $j_{\text{max}}$ ). The  $j_{\text{max}}$  value was  $\sim 33 \text{ mA cm}^{-2}$ , which is close to  $j_{\text{max}} = 31 \text{ mA cm}^{-2}$  obtained from the incident-photon-to-electron conversion efficiency (IPCE) spectrum recorded at 2 V vs RHE in 1 M NaOH (Figure S7). However, it has a notable influence on the OER slope (the part of the LSV located before the light-limited photocurrent plateau), which increases with decreasing  $p$ . This effect can be explained by the overall increase of the Ni surface area that enhances the OER kinetics and also reduces the series resistance of the Schottky junction device. Moreover, Figure 4a,b shows that the OER onset potential increases with  $p$ , suggesting that a too low density of Ni NWs and/or a high  $w$  is detrimental to the OER performance. However, this activity trend was qualitatively supported by dark/light open circuit potential (OCP) measurements performed in an aqueous solution containing the redox species  $\text{Fe}^{\text{III}}(\text{CN})_6^{3-}/\text{Fe}^{\text{II}}(\text{CN})_6^{4-}$  (Figure S8). The results showed that, under these conditions, the photovoltage ( $V_{\text{oc}}$ ) decreased from 426 to 392 mV with  $p$  increasing from 10 to 96  $\mu\text{m}$  (Figure 4c). Another interesting feature is the quasi-reversible wave that occurred before OER, as shown in Figure 4b for four *n*-Si/Ni NW photoanodes manufactured with different  $p$  values (30<sup>th</sup> CV cycle). This redox wave corresponds to the conversion of the outermost  $\text{Ni}^{\text{II}}(\text{OH})_2$  layer of the Ni NWs to  $\text{Ni}^{\text{III}}\text{OOH}$ <sup>50</sup>, and its magnitude depends on the number of *n*-Si/Ni NWs on the surface. Figure 4d shows a plot of the anodic charge ( $Q_{\text{Ni}}$ ; obtained by integration of the region before the forward scan peak) as a function of the Ni geometric area ( $A_{\text{Ni}}$ ), which was calculated using the previously determined geometrical parameters (Figure 3). These plots showed a linear correlation between these two parameters ( $R^2 = 0.982$ ), highlighting the good agreement between photoelectrochemical and characterization data. The slope of the linear fit indicated a charge density of  $3.9 \pm 0.2 \text{ mC cm}^{-2}$ , which agrees relatively well with the  $Q_{\text{Ni}}$  value determined on a 100 nm-thick planar Ni film ( $4.4 \text{ mC cm}^{-2}$ ) activated under similar conditions (Figure S9). The stability of the best *n*-Si/Ni NW photoanode ( $p = 10 \mu\text{m}$ , activated in 1 M NaOH) was tested by chronoamperometry (CA). As shown in Figure 4e, this surface could be operated in a moderately alkaline K-borate/Li-borate buffer (pH = 9.6, which is less basic than 1 M



NaOH) at 2.3 V vs RHE for 12 h without loss of performance, delivering an average photocurrent density of 31 mA cm<sup>-2</sup>, which is very close to the  $j_{\max}$  value (33 mA cm<sup>-2</sup>) determined from the LSVs shown in Figure 4a. Comparison with data reported on *n*-Si photoanodes modified by conventional electrodeposition of Ni nanoparticles (Figure S15a)<sup>32</sup> showed that these photoanodes have similar features, although they exhibit a higher OER onset potential and higher  $j_{\max}$ . These results showed that our approach allows for manufacturing stable OER *n*-Si-based photoanodes with high control over the Ni catalyst geometry and spacing. Moreover, we found that these geometrical features considerably influence the photoelectrochemical performance. Next, we report on our attempts to rationalize the measured photoelectrochemical trends.

### Rationalization of the photoelectrochemical trends

The fact that the best performance (Figure 4a), as well as the highest  $V_{oc}$  (Figure 4c), was obtained for the lowest  $p$  value is counterintuitive at first. Indeed, as discussed in the introduction, increasing the number of Ni NWs per electrode should increase the area of low barrier height *n*-Si/Ni contacts ( $q\phi_m$ ; Figure 1b) and, thus, decrease  $q\phi_{eff}$  in a first approximation, which is correlated to a decrease of the photoanode performance and opposite to our results. To rationalize our experimental results, we performed 2D electrical numerical simulations applying a finite volume method using the commercial TCAD software Silvaco (details are given in the Supporting Information). These simulations provided the following key photovoltaic parameters: reverse dark current density ( $j_{0,dark}$ ), short circuit photocurrent density ( $j_{sc}$ ),  $V_{oc}$ , and fill factor (FF). Our simulations employed a model comprising low barrier height regions (i.e., *n*-Si/Ni contacts) spaced by high barrier height regions with the corresponding work functions ( $W$ ), which were chosen to define barrier height values in the range reported for metal-covered and metal-uncovered regions.<sup>37,51</sup> Even though this latter phase is, literally, not the liquid because it does not include information about the electrolyte potential, for the sake of simplicity, it is referred to here as the "electrolyte" in the sense that it is the metal-uncovered part of the photoelectrode.

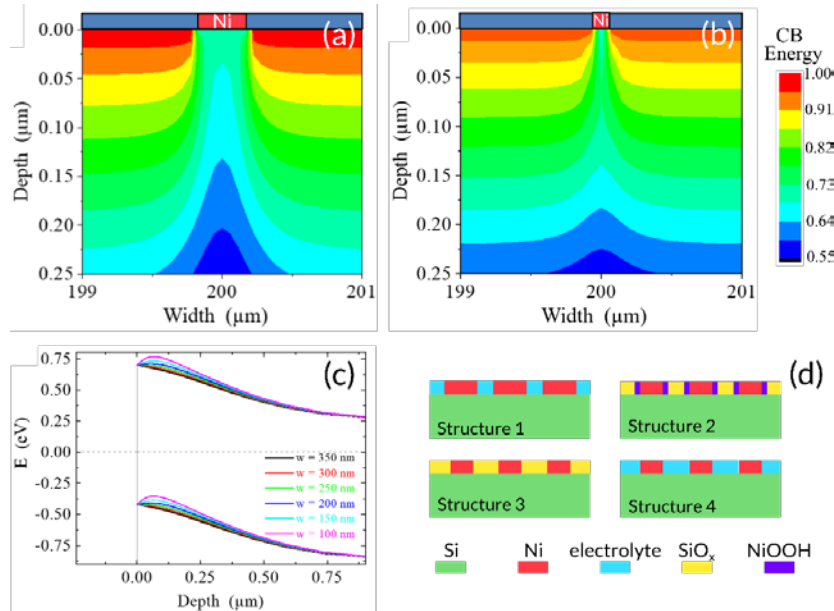


**Figure 5.** (a,b) 2D representation of the CB energy in *n*-Si for an *n*-Si/Ni surface with  $p=100\ \mu\text{m}$  and (a)  $w=350\ \text{nm}$  (black) and (b)  $w=100\ \text{nm}$ . (c) Graph of the band bending below a Ni pad for a surface with  $p=100\ \mu\text{m}$  for  $w=350$  (black), 300 (red), 250 (green), 200 (blue), 150 (cyan), and 100 (purple) nm. These energy band profiles are extracted from a cutline located in the middle of the centered Ni pad. Zero depth represents the position of the silicon interface. (d) Schemes of the surface models that have been computed. Their key photovoltaic parameters are reported in Table 1 as a function of their geometrical parameters. The Ni pad electrode widths  $w$  of Structures 2, 3, and 4 are reduced by 50 nm compared to those of Structure 1.

**Table 1.** Key photovoltaic parameters extracted from simulated J-V curves under AM 1.5 G illumination for Structures 1-4 shown in Figure 5d.

Geometrical parameters $p$ ( $\mu\text{m}$ ), $w$ (nm), pads#	Structure 1 Si-Ni		Structure 2 Si-SiO <sub>x</sub> -Ni-NiOOH		Structure 3 Si-SiO <sub>x</sub> -Ni		Structure 4 Si-Ni	
	$j_{sc}$ mA cm <sup>-2</sup>	$V_{oc}$ V	$j_{sc}$ mA cm <sup>-2</sup>	$V_{oc}$ V	$j_{sc}$ mA cm <sup>-2</sup>	$V_{oc}$ V	$j_{sc}$ mA cm <sup>-2</sup>	$V_{oc}$ V
100, 350, 2	23.854	0.372						
50, 300, 3	23.831	0.371						
25, 230, 5	23.800	0.375						
10, 180, 11	23.701	0.377						
100, 300, 2			29.405	0.389	29.414	0.369	23.866	0.385
50, 250, 3			29.380	0.391	29.392	0.367	23.848	0.385
25, 180, 5			29.375	0.399	29.387	0.370	23.829	0.399
10, 130, 11			29.301	0.402	29.305	0.370	23.763	0.402

Our first model comprised 3 metal pads (representing Ni NW sections) spaced on a 400  $\mu\text{m}$ -large  $n$ -Si surface with  $w$  and associated  $p$  dimensions that were consistent with our experiments. The results reported in Table S1 demonstrate that the shading effect induced a negligible decrease in the light-limited photocurrent density (which was, in this case, smaller than our experimental  $j_{\text{max}}$  values, as will be discussed later). This also showed that  $V_{oc}$  increased with decreasing  $p$  and  $w$  due to the change in reverse dark current density ( $j_{0,\text{dark}}$ ) associated with the increasing  $n$ -Si/Ni contact area. This model structure was also used to picture the Si energetics around a Ni pad. **Figure 5a,b** shows the models as 2D representations of the conduction band (CB) energy for  $p = 100 \mu\text{m}$  and extreme  $w$  values of 350 and 100 nm, respectively. These data show the considerable impact of  $w$  on the band bending profile close to the surface (see the supplementary information for more details). This is also clearly illustrated in Figure 5c, which shows the 1D band bending (conduction and valence bands) below a Ni pad with a  $p$  value fixed at 100  $\mu\text{m}$  and varying pad width (100 nm <  $w$  < 350 nm). These figures clearly show that shrinking the Ni NW section increases the effective barrier height, which is in good agreement with the literature devoted to the pinch-off phenomenon.<sup>35,44,45</sup> Importantly, the change of  $p$  in the 10–100  $\mu\text{m}$  range had no significant impact on the Si band bending. According to our simulation, an impact will be only observed for  $p < 0.5 \mu\text{m}$  (in the range of  $w$  used here), which falls below the reachable range of our experimental study.

To better understand the photoelectrochemical results in Figure 4, we tested a set of more sophisticated model structures, shown in Figure 5d. Here, 200  $\mu\text{m}$ -wide  $n$ -Si surfaces were entirely covered by metal pads with  $p/w$  set values of 100  $\mu\text{m}/350 \text{ nm}$ , 50  $\mu\text{m}/300 \text{ nm}$ , 25  $\mu\text{m}/230 \text{ nm}$ , and 10  $\mu\text{m}/180 \text{ nm}$ , which were coherent with experimentally determined values (Figure 3h). The values of  $j_{sc}$  and  $V_{oc}$  of each system are reported in **Table 1**. The first model that was tested (Figure 5d, Structure 1) is similar to that used for Figure 5c (see also Table S1) but comprises a higher and more realistic NW surface coverage. Tables 1 and S2 show that this structure exhibited a smaller but coherent evolution of  $V_{oc}$  with the geometrical parameters. However, the  $j_{sc}$  values ( $\sim 24 \text{ mA cm}^{-2}$ ) were lower than the experimentally determined  $j_{\text{max}}$  (31 to 33  $\text{mA cm}^{-2}$ ; Figures 3a and S7). Another structure model that was computed comprised additional surface oxide layers, namely SiO<sub>x</sub> and NiOOH, which are known to appear at the Si and the Ni surface, respectively, during the operation as photoanodes (as discussed previously, Figure 4b).<sup>32,50</sup> Here, a 2 nm-thick SiO<sub>x</sub> layer and 25 nm-wide NiOOH layers, present at both edges of the Ni pads, were added to our model (Figure 5d, Structure 2). As shown in Table 1, the modeling results of Structure 2 were in better agreement with our experimental results, and  $j_{sc}$  was much higher ( $\sim 29 \text{ mA cm}^{-2}$ ) with a stronger  $V_{oc}$  increase. Finally, to elucidate the effect of each coating, two control structures (Figure 5d, Structures 3,4) were also

computed. As illustrated in Figure 5d, these control surfaces were geometrically identical to Structure 2, but Structure 3 did not contain NiOOH, and Structure 4 contained neither NiOOH nor SiO<sub>x</sub> coating. The results shown in Table 1 demonstrate that Structures 3 and 4 lead to tendencies that are farther from our experimental results. Indeed, if the presence of SiO<sub>x</sub> imposes a high  $j_{sc}$  (Supporting Information, Table S3), it does not promote the variation of  $V_{oc}$  (~0.37 V). Moreover, shrinking of the Ni pad width due to the presence of NiOOH improves the  $V_{oc}$  trend but does not lead to relevant  $j_{sc}$  values. To sum up, our simulation approach allows us to qualitatively understand the experimental results obtained in the photoelectrochemical experiments. In particular, it showed that the decrease of the width of the Ni NW due to oxidation to NiOOH is likely a key parameter that increases  $V_{oc}$  and thus decreases the onset potential (Figure 4a,b). Conversely,  $p$  has a very small influence on  $V_{oc}$  in our length scale. Furthermore, our simulations highlight the importance of the SiO<sub>x</sub> layer in promoting a high photocurrent density.

## Conclusions

To conclude, we have proposed an original electrodeposition approach for the preparation of tailored inhomogeneous  $n$ -Si/M NW Schottky junctions, and we have demonstrated that these surfaces can be used as reliable photoanodes for OER in alkaline solution. This method allows the unprecedented control of the geometrical parameters of nanoscale metal contacts (i.e., Ni, Co, and Fe), which act as hole collectors as well as catalytically active sites for the electrochemical reaction. Our measurements revealed that the photoelectrochemical properties of the manufactured photoanodes were strongly dependent on the photoanodes' geometrical features, and the obtained experimental trends were rationalized by a qualitative simulation approach. In particular, our results are consistent with the existence of a high barrier height region originating from the contact between  $n$ -Si and a metal oxide or oxyhydroxide phase on the NWs. We believe that this electroplating method has the potential to provide important insights into inhomogeneous pinched-off photoanodes, for which geometric control at the nanoscale is a crucial aspect.<sup>34,37</sup> For future studies, it would be relevant to adapt the process to e-beam lithography methods to electroplate catalysts separated by a shorter distance (<1  $\mu$ m). Furthermore, elucidating the effect of the plated transition metal will bring considerable progress, which should soon be revealed as this process has proven to be very versatile. With the provided degree of control, this approach has the potential to achieve a deep understanding of physicochemical parameters, which could open new avenues in the development of efficient solar-to-fuel conversion photoelectrodes.

## Author Contributions

GL conceived and planned the experiments. OS prepared the templates. KO prepared the samples and performed the experiments. SLG performed the modeling and the numerical simulation with the help of CL. The manuscript was written through the contributions of all authors. All authors have approved the final version of the manuscript.

## Conflicts of interest

There are no conflicts to declare.

## Acknowledgements

This work was funded by ANR (project EASi-NANO, ANR-16-CE09-0001-01). Loïc Joanny and Francis Gouttefangeas from ScanMAT/CMEBA are warmly acknowledged for SEM analyses. Bruno Fabre and Jean-François Bergamini are also acknowledged for fruitful discussions. ScienceScripts.net is

acknowledged for the help with the edition of the manuscript. A part of the microfabrication process has been performed at NanoRennes.

## References

- N. S. Lewis and D. G. Nocera, *Proc. Natl. Acad. Sci.*, 2006, **103**, 15729–15735.
- D. Abbott, *Proc. IEEE*, 2010, **98**, 42–66.
- H. Gerischer, in *Solar Energy Conversion: Solid-State Physics Aspects*, ed. B. O. Seraphin, Springer, Berlin, Heidelberg, 1979, pp. 115–172.
- M. G. Walter, E. L. Warren, J. R. McKone, S. W. Boettcher, Q. Mi, E. A. Santori and N. S. Lewis, *Chem. Rev.*, 2010, **110**, 6446–6473.
- R. van de Krol and M. Grätzel, *Photoelectrochemical Hydrogen Production*, Springer, New York, 2012.
- J. W. Ager, M. R. Shaner, K. A. Walczak, I. D. Sharp and S. Ardo, *Energy Environ. Sci.*, 2015, **8**, 2811–2824.
- K. Sivula and R. van de Krol, *Nat. Rev. Mater.*, 2016, **1**, 15010.
- M. S. Prévot and K. Sivula, *J. Phys. Chem. C*, 2013, **117**, 17879–17893.
- J. Tournet, Y. Lee, S. K. Karuturi, H. H. Tan and C. Jagadish, *ACS Energy Lett.*, 2020, **5**, 611–622.
- K. Sun, S. Shen, Y. Liang, P. E. Burrows, S. S. Mao and D. Wang, *Chem. Rev.*, 2014, **114**, 8662–8719.
- Z. Luo, T. Wang and J. Gong, *Chem. Soc. Rev.*, 2019, **48**, 2158–2181.
- D. Bae, B. Seger, P. C. K. Vesborg, O. Hansen and I. Chorkendorff, *Chem. Soc. Rev.*, 2017, **46**, 1933–1954.
- X. G. Zhang, *Electrochemistry of Silicon and Its Oxide*, Kluwer Academic, 2001.
- C. C. L. McCrory, S. Jung, I. M. Ferrer, S. M. Chatman, J. C. Peters and T. F. Jaramillo, *J. Am. Chem. Soc.*, 2015, **137**, 4347–4357.
- S. A. Lee, S. Choi, C. Kim, J. W. Yang, S. Y. Kim and H. W. Jang, *ACS Mater. Lett.*, 2020, **2**, 107–126.
- K. Jun, Y. S. Lee, T. Buonassisi and J. M. Jacobson, *Angew. Chemie Int. Ed.*, 2011, **51**, 423–427.
- M. J. Kenney, M. Gong, Y. Li, J. Z. Wu, J. Feng, M. Lanza and H. Dai, *Science* 2013, **342**, 836–840.
- 18 S. Hu, M. R. Shaner, J. A. Beardslee, M. Lichterman, B. S. Brunschwig and N. S. Lewis, *Science* 2014, **344**, 1005–1009.
- Z. Luo, B. Liu, H. Li, X. Chang, W. Zhu, T. Wang and J. Gong, *Small Methods* 2019, **0**, 1900212.
- A. G. Scheuermann, J. P. Lawrence, K. W. Kemp, T. Ito, A. Walsh, C. E. D. Chidsey, P. K. Hurley and P. C. McIntyre, *Nat. Mater.* 2016, **15**, 99–105.
- I. A. Digdaya, B. J. Trzeźniewski, G. W. P. Adhyaksa, E. C. Garnett and W. A. Smith, *J. Phys. Chem. C* 2018, **122**, 5462–5471.
- X. Zhou, R. Liu, K. Sun, K. M. Papadantonakis, B. S. Brunschwig and N. S. Lewis, *Energy Environ. Sci.* 2016, **9**, 892–897.

Y. Li, G. Xu, X. Zhu, Z. Man, X. Fu, Z. Hao, Y. Cui, C. Yuan, W. Zhang, S. Yan, H. Ge, Y. Chen and Z. Zou, *Appl. Catal. B Environ.*, 2019, **259**, 118115.

G. Loget, *Curr. Opin. Colloid Interface Sci.*, 2019, **39**, 40-50.

G. Loget, B. Fabre, S. Fryars, C. Mériadec and S. Ababou-Girard, *ACS Energy Lett.*, 2017, **2**, 569–573.

S. A. Lee, T. H. Lee, C. Kim, M. G. Lee, M.-J. Choi, H. Park, S. Choi, J. Oh and H. W. Jang, *ACS Catal.*, 2018, **8**, 7261–7269.

C.-W. Tung, T.-R. Kuo, C.-S. Hsu, Y. Chuang, H.-C. Chen, C.-K. Chang, C.-Y. Chien, Y.-J. Lu, T.-S. Chan, J.-F. Lee, J.-Y. Li and H. M. Chen, *Adv. Energy Mater.* 2019, **9**, 1901308.

K. Oh, L. Joanny, F. Gouttefangeas, B. Fabre, V. Dorcet, B. Lassalle-Kaiser, A. Vacher, C. Mériadec, S. Ababou-Girard and G. Loget, *ACS Appl. Energy Mater.*, 2019, **2**, 1006–1010.

J. C. Hill, A. T. Landers and J. A. Switzer, *Nat. Mater.*, 2015, **14**, 1150–1155.

S. A. Lee, T. H. Lee, C. Kim, M.-J. Choi, H. Park, S. Choi, J. Lee, J. Oh, S. Y. Kim and H. W. Jang, *ACS Catal.*, 2020, **10**, 420–429.

K. Oh, V. Dorcet, B. Fabre and G. Loget, *Adv. Energy Mater.*, 2020, **10**, 1902963.

K. Oh, C. Mériadec, B. Lassalle-Kaiser, V. Dorcet, B. Fabre, S. Ababou-Girard, L. Joanny, F. Gouttefangeas and G. Loget, *Energy Environ. Sci.*, 2018, **11**, 2590–2599.

G. Xu, Z. Xu, Z. Shi, L. Pei, S. Yan, Z. Gu and Z. Zou, *ChemSusChem*, 2017, **10**, 2897–2903.

R. C. Rossi, N.S. Lewis, *J. Phys. Chem. B* 2001, **105**, 12303–12318.

R. T. Tung, *App. Phys. Rev.*, 2014, **1**, 011304.

F. A. L. Laskowski, M. R. Nellist, R. Venkatkarthick and S. W. Boettcher, *Energy Environ. Sci.*, 2017, **10**, 570–579.

F. A. L. Laskowski, S. Z. Oener, M. R. Nellist, A. M. Gordon, D. C. Bain, J. L. Fehrs and S. W. Boettcher, *Nat. Mater.*, 2020, **19**, 69–76.

E. J. Menke, M. A. Thompson, C. Xiang, L. C. Yang and R. M. Penner, *Nat Mater*, 2006, **5**, 914–919.

J. E. Hujdic, A. P. Sargisian, J. Shao, T. Ye and E. J. Menke, *Nanoscale*, 2011, **3**, 2697–2699.

C. Xiang, S.-C. Kung, D. K. Taggart, F. Yang, M. A. Thompson, A. G. Güell, Y. Yang and R. M. Penner, *ACS Nano*, 2008, **2**, 1939–1949.

G. Loget and R. M. Corn, *Chem. - A Eur. J.*, 2014, **20**, 10802–10810.

H.-J. Cho, V. T. Chen, S. Qiao, W.-T. Koo, R. M. Penner and I.-D. Kim, *ACS Sensors*, 2018, **3**, 2152–2158.

M. Le Thai, G. T. Chandran, R. K. Dutta, X. Li and R. M. Penner, *ACS Energy Lett.*, 2016, **1**, 57–63.

R. T. Tung, *Appl. Phys. Lett.*, 1991, **58**, 2821–2823.

J. P. Sullivan, R. T. Tung, M. R. Pinto and W. R. Graham, *J. Appl. Phys.*, 1991, **70**, 7403–7424.

R. Balsano, A. Matsubayashi and V. P. LaBella, *AIP Adv.*, 2013, **3**, 112110.

D. A. Corrigan, *J. Electrochem. Soc.*, 1987, **134**, 377–384.

- M. B. Stevens, L. J. Enman, A. S. Batchellor, M. R. Cosby, A. E. Vise, C. D. M. Trang and S. W. Boettcher, *Chem. Mater.*, 2017, **29**, 120–140.
- S. L. Medway, C. A. Lucas, A. Kowal, R. J. Nichols and D. Johnson, *J. Electroanal. Chem.*, 2006, **587**, 172–181.
- D. S. Hall, C. Bock and B. R. MacDougall, *J. Electrochem. Soc.* , 2013, **160**, F235–F243.
- G. Loget, C. Mériadec, V. Dorcet, B. Fabre, A. Vacher, S. Fryars and S. Ababou-Girard, *Nat. Commun.* **2019**, *10*, 3522.